Inorganic Chemistry

Article

pubs.acs.org/IC

Syntheses and Characterization of Six Quaternary Uranium Chalcogenides $A_2M_4U_6Q_{17}$ (A = Rb or Cs; M = Pd or Pt; Q = S or Se)

George N. Oh,[†] Eun Sang Choi,[‡] Jun Lu,[‡] Lukasz A. Koscielski,[†] Matthew D. Ward,[†] Donald E. Ellis,[§,†] and James A. Ibers[†,*]

[†]Department of Chemistry, Northwestern University, 2145 Sheridan Road, Evanston, Illinois 60208-3113, United States

[‡]Department of Physics and National High Magnetic Field Laboratory, Florida State University, Tallahassee, Florida, 32310-3706, United States

[§]Department of Physics and Astronomy, Northwestern University, 2145 Sheridan Road, Evanston, Illinois 60208-3112, United States

S *Supporting Information*

ABSTRACT: The $A_2M_4U_6Q_{17}$ compounds $Rb_2Pd_4U_6S_{17}$, $Rb_2Pd_4U_6Se_{17}$, $Rb_2Pt_4U_6Se_{17}$, $Cs_2Pd_4U_6S_{17}$, $Cs_2Pd_4U_6Se_{17}$, and $Cs_2Pt_4U_6Se_{17}$ were synthesized by the high-temperature solid-state reactions of U, M, and Q in a flux of ACl or Rb_2S_3. These isostructural compounds crystallize in a new structure type, with two formula units in the tetragonal space group *P*4/*mnc*. This structure consists of a network of square-planar MQ_4, monocapped trigonal-prismatic UQ_7, and square-antiprismatic UQ_8 polyhedra with A atoms in the voids. $Rb_2Pd_4U_6S_{17}$ is a typical semiconductor, as deduced from electrical resistivity measurements. Magnetic susceptibility and specific heat measurements on single crystals of $Rb_2Pd_4U_6S_{17}$ show a phase transition at 13 K, the result either of antiferromagnetic ordering or of a structural phase transition. Periodic spin-polarized band structure calculations were performed on $Rb_2Pd_4U_6S_{17}$ with the use of the first principles DFT program VASP. Magnetic calculations included spin−orbit coupling. With U f-f correlations taken into account within the GGA+U formalism in calculating partial densities of states, the compound is predicted to be a narrow-band semiconductor with the smallest indirect and direct band gaps being 0.79 and 0.91 eV, respectively.

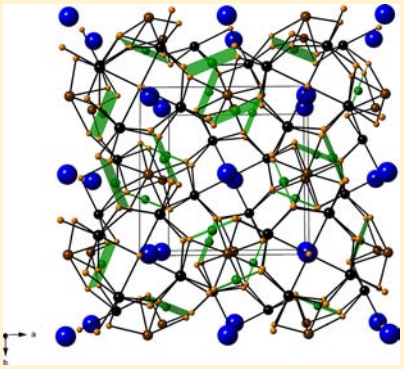

INTRODUCTION

Compounds containing both uranium and a chalcogen display varied physical properties, especially magnetic behavior, depending on the interatomic U···U distances and the coordination environment of U. The U···U distances affect whether or not long-range magnetic ordering occurs, whereas the coordination environment produces an array of effects collectively referred to as crystalline electric field effects. Exploration of the ternary and quaternary uranium chalcogenide systems has yielded compounds that differ in the values of these two parameters, but there remain many unexplored combinations. The strong preference for square-planar coordination of the platinum-group metals offers a way to affect the coordination environment of U, especially when the MQ_4 units edge-share with the U-containing polyhedra.

We recently reported a series of quaternary uranium palladium and platinum chalcogenides, $A_2M_3UQ_6$ (A = K, Rb, Cs; M = Pd, Pt; Q = S, Se),[1,2] which crystallize in the $NaBa_2Cu_3O_6$ structure type.[3] These compounds contain square-planar $PdSe_4$ or $PtSe_4$ units that edge-share with trigonal-prismatically coordinated USe_6 units. This coordination environment for U was found in another chalcogenide compound, $Ba_4Cr_2US_9$,[4] and a distorted version of this coordination environment was found in $Cs_8Hf_5UTe_{30.6}$.[5]

There appear to be no examples of ternary compounds containing Pt, U, and Q (Q = S, Se, or Te). With the exception of the $A_2M_3UQ_6$ compounds, there are no examples of quaternary compounds containing Pd or Pt, U, and Q. To take further advantage of the unique coordination environments available to Pd and Pt, we have synthesized and characterized six new quaternary $A_2M_4U_6Q_{17}$ compounds, and we report the results here.

EXPERIMENTAL METHODS

Syntheses. U filings (Oak Ridge National Laboratory) were powdered by hydridization and subsequent decomposition under heat and vacuum[6] in a modification of a previous literature method.[7] Rb_2S_3 flux was synthesized by the stoichiometric reaction of Rb (Strem, 99%) and S (Mallinckrodt, 99.6%) in liquid ammonia at 194 K.[8] All other reagents were used as obtained: Pd (Johnson Matthey, 99.94%), Pt wire (Omega Engineering, 0.25 mm diameter, 99.95%), RbCl (Alfa, 99.8%), CsCl (two batches: (1) Aldrich, 99.9%; (2) MP Biomedicals, 99.9% Optical grade), and Se (Cerac, 99.999%).

All reactants were loaded into 6 mm inner-diameter carbon-coated fused-silica tubes in an argon-filled glovebox. The tubes were removed, and then flame-sealed under 10^{-3} Torr vacuum. They were then placed in a computer-controlled furnace and heated as detailed below. The crystals are black, hard, brittle, and air- and water-stable. They

Received: April 27, 2012
Published: August 3, 2012

   dx.doi.org/10.1021/ic300865y | *Inorg. Chem.* 2012, 51, 8873−8881

Table 1. Crystal Data and Structure Refinements[a]

	$Cs_2Pt_4U_6Se_{17}$	$Cs_2Pd_4U_6Se_{17}$	$Cs_2Pd_4U_6S_{17}$	$Rb_2Pt_4U_6Se_{17}$	$Rb_2Pd_4U_6Se_{17}$	$Rb_2Pd_4U_6S_{17}$
fw (g mol^{-1})	3816.68	3461.92	2664.62	3721.8	3367.04	2569.74
a (Å)	10.6744(3)	10.7732(2)	10.4277(1)	10.5591(1)	10.6730(2)	10.3218(1)
c (Å)	13.3691(4)	13.3032(2)	12.7769(2)	13.4043(2)	13.2822(2)	12.7302(3)
V (Å^3)	1523.31(8)	1543.99(5)	1389.32(3)	1494.51(3)	1513.01(5)	1356.27(4)
ρ_c (g cm^{-3})	8.321	7.446	6.37	8.271	7.391	6.292
μ (mm^{-1})	72.714	55.968	41.206	74.95	57.939	43.131
$R(F)^b$	0.0206	0.0280	0.0148	0.0304	0.0165	0.0211
$R_w(F_o^2)^c$	0.0396	0.0700	0.0305	0.0630	0.0377	0.0526
q^c	0.0167	0.022	0.0136	0.0309	0.0123	0.0106

[a]For all structures, T = 100(2) K, λ = 0.71073 Å, Z = 2, and the space group is $D_{4h}^6 - P4/mnc$. [b]$R(F) = \Sigma||F_o| - |F_c||/\Sigma|F_o|$ for $F_o^2 > 2\sigma(F_o^2)$. [c]$R_w(F_o^2) = \{\Sigma\, w(F_o^2 - F_c^2)^2/\Sigma\, wF_o^4\}^{1/2}$. For $F_o^2 < 0$, $w^{-1} = \sigma^2(F_o^2)$; for $F_o^2 \geq 0$, $w^{-1} = \sigma^2(F_o^2) + (qF_o^2)^2$.

Table 2. Selected Interatomic Distances (Å) for $A_2U_6M_4Q_{17}$[a]

	$Cs_2Pt_4U_6Se_{17}$	$Cs_2Pd_4U_6Se_{17}$	$Cs_2Pd_4U_6S_{17}$	$Rb_2Pt_4U_6Se_{17}$	$Rb_2Pd_4U_6Se_{17}$	$Rb_2Pd_4U_6S_{17}$
U1−Q2 × 2	2.8144(6)	2.7996(4)	2.678(1)	2.8201(7)	2.8011(5)	2.680(1)
U1−Q1 × 2	2.8891(6)	2.8980(4)	2.786(1)	2.8877(6)	2.8927(5)	2.777(1)
U1−Q3	2.9080(3)	2.8969(2)	2.8021(2)	2.9040(3)	2.8965(3)	2.7968(3)
U1−Q1 × 2	2.9657(6)	2.9601(4)	2.834(1)	2.9564(6)	2.9502(5)	2.823(1)
U2−Q2 × 4	2.8932(5)	2.8764(3)	2.753(1)	2.9166(6)	2.8947(5)	2.762(1)
U2−Q1 × 4	3.0003(5)	3.0263(3)	2.924(1)	2.9717(6)	2.9960(5)	2.887(1)
M1−Q2 × 2	2.4708(6)	2.4574(4)	2.342(1)	2.4709(7)	2.4586(6)	2.341(1)
M1−Q1 × 2	2.4748(5)	2.4766(4)	2.364(1)	2.4829(7)	2.4805(6)	2.363(1)
A1−Q2 × 4	3.4850(8)	3.4530(4)	3.359(1)	3.418(1)	3.3758(6)	3.279(1)
A1−Q1 × 4	2.5100(8)	3.6924(4)	3.634(1)	3.433(1)	3.6283(7)	3.573(2)
A1−Q3	3.416(1)	3.7276(5)	3.6442(5)	3.370(2)	3.676(1)	3.589(1)
A2−Q2 × 4[b]	3.4054(7)			3.332(1)		
A2−Q2 × 4[b]	3.8381(9)			3.731(2)		
Q−Q (shortest)	3.4231(7)	3.4553(5)	3.305(2)	3.4063(9)	3.4426(7)	3.300(2)

[a]Atoms have the following site symmetries: U1 (m); U2 (2.22); M1 (m); A1 ($\bar{4}$); A2 ($\bar{4}$); Q1 (1); Q2 (1); Q3 (4/m..). [b]Only found in compounds with alkali-metal positional disorder.

were washed with water or DMF, except where noted. EDS analyses on single crystals with a Hitachi S-3400 SEM indicated the presence of the four elements appropriate for each compound and no perceptible amount of others.

$Rb_2Pd_4U_6S_{17}$. A mixture of U (0.126 mmol), Pd (0.378 mmol), S (0.504 mmol), and RbCl (1.260 mmol) was heated to 1023 K in 96 h, held there for 192 h, cooled to 723 K in 96 h, then cooled to 298 K in 98 h to yield small, truncated, rectangular prisms in 5−10 wt % (based on U). A single crystal was selected for the X-ray diffraction determination of the structure. In another preparation, a mixture of U (0.126 mmol), Pd (0.084 mmol), S (0.504 mmol), Rb_2S_3 (0.042 mmol), and RbCl (1.654 mmol) was heated to 1023 K in 96 h, held there for 192 h, cooled to 873 K in 96 h, cooled to 723 K in 96 h, then cooled to 298 K in 24 h to afford small crystals and several large rectangular blocks suitable for single-crystal magnetic susceptibility measurements in about 50 wt % yield.

$Rb_2Pd_4U_6Se_{17}$. A mixture of U (0.084 mmol), Pd (0.252 mmol), Se (0.504 mmol), and RbCl (1.008 mmol) was heated to 1223 K in 48 h, held there for 192 h, cooled to 773 K in 96 h, then cooled 298 K in 98 h to yield tapered needles and rectangular prisms in 5−10 wt % yield. Crystals were mechanically separated from the melt.

$Rb_2Pt_4U_6Se_{17}$. A mixture of Rb_2Se_3 (0.126 mmol), U (0.126 mmol), Pt (0.126 mmol), and Se (0.504 mmol) was heated to 1223 K in 96 h, held there for 192 h, cooled to 773 K in 96 h, then cooled to 298 K in 24 h to yield a few tapered black needles of $Rb_2U_6Pt_4Se_{17}$. $Rb_2Pt_3USe_6$ was synthesized in the same tube at about 20 wt % by U.[2]

$Cs_2Pd_4U_6S_{17}$. A mixture of U (0.084 mmol), Pd (0.252 mmol), S (0.504 mmol), and CsCl (1) (1.008 mmol) was heated to 1273 K in 48 h, held there for 24 h, cooled to 1173 K in 96 h, cooled to 673 K in 288 h, then cooled to 298 K in 96 h to yield rectangular prisms in 5−10 wt % yield.

$Cs_2Pd_4U_6Se_{17}$. A mixture of U (0.126 mmol), Pd (0.126 mmol), Se (0.378 mmol), and CsCl (2) (0.445 mmol) was heated to 1173 K in 12 h, held there for 6 h, cooled to 1073 K in 12 h, and held there for over 96 h. The furnace was then shut off and allowed to come to room temperature to yield large tetragonal prisms in about 70−80 wt % yield.

$Cs_2Pt_4U_6Se_{17}$. A mixture of U (0.126 mmol), Pt (0.126 mmol), Se (0.378 mmol), and CsCl (2) (0.445 mmol), heated as for $Cs_2Pd_4U_6Se_{17}$, afforded small tetragonal prisms, along with large amounts of microcrystalline powder of $Cs_2Pt_4U_6Se_{17}$ in about 70−80 wt % yield.

Structure Determinations. For $Rb_2Pd_4U_6S_{17}$, $Rb_2Pd_4U_6Se_{17}$, $Rb_2Pt_4U_6Se_{17}$, and $Cs_2Pd_4U_6S_{17}$, X-ray diffraction data were collected from single crystals on a Bruker APEXII platform diffractometer. The data were collected as ω scans at ϕ values of 0°, 90°, 180°, and 270°. Each scan consisted of 606 frames. The counting times were 15 s/frame for $Cs_2Pd_4U_6S_{17}$, 10 s/frame for $Rb_2Pd_4U_6Se_{17}$ and $Rb_2Pd_4U_6S_{17}$, and 20 s/frame for $Rb_2Pt_4U_6Se_{17}$. For $Cs_2Pd_4U_6Se_{17}$ and $Cs_2Pt_4U_6Se_{17}$, data were collected on a Bruker APEXII KAPPA diffractometer, and collection strategies were devised using COSMO in APEX2.[9] Counting times were 10 s/frame and 30 s/frame, respectively. For all compounds, the detector distance was 60 mm, frames were 0.3° in width, and the initial 50 frames were recollected at the end to check for crystal degradation—none was noted. Cell refinements and data reductions were carried out with SAINT in APEX2.[9] Examination of the data showed no evidence for supercells. Numerical face-indexed absorption corrections were applied using SADABS.[10] Structure determinations were carried out by direct methods with XS and least-squares refinements were carried out with XL of the SHELX[11] package. Secondary corrections for extinction were applied. The atomic positions were standardized using STRUCTURE TIDY[12] in PLATON.[13] Crystallographic details are

dx.doi.org/10.1021/ic300865y | Inorg. Chem. 2012, 51, 8873−8881

given in Table 1, and selected metrical details are given in Table 2. Additional information is in the Supporting Information.

Magnetic Measurements. A large crystal of $Rb_2Pd_4U_6S_{17}$ was selected for magnetic measurements. It was washed with DMF and water, and then large surface impurities were mechanically removed under oil. It was rinsed with hexanes, briefly soaked in concentrated HNO_3 to remove smaller impurities, rinsed with water, and then with acetone. The rectangular-parallelpiped-shaped crystal had a mass of 4.0 mg. The crystal faces were indexed by diffraction measurements on a small piece of crystal that was broken off the large crystal. The two basal plane axes are crystallographically equivalent, and the *a* and *b* axis are arbitrarily assigned to the medium and shortest edges of the crystal, respectively.

Detailed magnetic susceptibility measurements were taken on a Quantum Design MPMS XL-7 SQUID magnometer. The crystal was glued to a quartz rod with GE7031 varnish. Both field-cooled and zero-field cooled magnetic susceptibility data were collected. The results were identical, ruling out ferromagnetism. Measurements were taken along the three crystallographic axes. Magnetization data as a function of external field were also collected. The crystal was mounted on a horizontal rotator probe to study the angular dependence at fixed temperatures and external fields.

Electrical Resistivity Measurements. The electrical resistivity of the crystal used in magnetic measurements was measured with standard four-probe techniques. Four Au wires were attached with carbon paint along the *c* axis. A Keithley 6221 current source and a Keithley 2182 nanovoltmeter were used to measure the resistivity. A total of 50 nA of alternating current was applied using the current source, and the voltage drop was measured using the nanovoltmeter.

Specific Heat Measurements. The same crystal was used in specific heat measurements. The specific heat was measured using a Quantum Design PPMS by gluing the crystal on the platform with a thin layer of grease. An addendum including the platform and grease was measured beforehand. The specific heat was measured under high vacuum by fitting the temperature response to a heat pulse and subtracting the addendum.

Theoretical Calculations. As a simple empirical measure of oxidation state, bond valences were calculated for $Rb_2Pd_4U_6S_{17}$ from standard parameters.[14] The bond valence of an atom, *V*, is defined as the sum of the individual bond valences, v_i, surrounding the atom: $V = \sum v_i$. Individual bond valences were calculated from experimental bond lengths, R_i, and empirical parameters, R_0, which are unique to each atom pair: $v_i = \exp[(R_0 - R_i)/0.37]$. The parameter R_0 for the atom pairs U−S, Pd−S, and Rb−S was 2.56, 2.10, and 2.70 Å, respectively.[14]

Periodic spin-polarized band structure calculations were performed on $Rb_2Pd_4U_6S_{17}$ with the use of the first principles DFT program VASP (Vienna ab initio simulation package); pseudopotentials were applied with a plane-wave basis.[15−18] The exchange correlation potential was chosen as the generalized gradient approximation (GGA) in a projector augmented wave (PAW) method.[19] Some additional self-consistent field (SCF) calculations also included spin−orbit coupling (SOC) to explore effects on energy bands, cohesive energy, and magnetic structures. In order to treat effects of intra-atomic U 5f correlations on band gaps, some post-SCF calculations were performed in the GGA+U formalism.[20] Automatically generated Monkhorst−Pack grids were used to carry out Brillouin zone integrations.[21] Additionally, 5 × 5 × 5 *k*-point meshes were chosen for relaxations, total energy calculations, establishing convergence, energy comparisons, and DOS analysis. Ionic relaxation convergence was established when Hellmann−Feynmann forces on each ion relaxed below 0.02 eV/Å. With inclusion of SOC, the spin density was now coupled to the orbital angular momentum; hence, the positive (α) and negative (β) magnetization densities were coupled to the lattice vectors, and both spin (M_S) and orbital (M_L) contributions to the total magnetization (M_J) were calculated. The point group symmetry of the noncollinear magnetic moments was maintained as C_{1h} in all SOC calculations.[22]

In the calculations, the electrons described as core in the PAW potentials were those composed of [Xe] $5d^{10}4f^{14}$ for U, leaving 14 valence elections per atom as 5f ^{3}6s^{2}p^{6}d^{1}7s^2; [Ar] $3d^{10}4s^2$ for Pd, leaving 16 valence electrons as $4p^6d^{10}$; [Ar] $3d^{10}4s^2$ for Rb, leaving seven valence electrons as $4p^65s^1$; and [Ne] for S, leaving six valence electrons as $3s^2p^4$. Calculations were conducted on the 68-atom periodic crystallographic unit cell in the tetragonal space group *P*4/*mnc*; atomic positions within the fixed 100 K unit cell were relaxed to their lowest energy positions.

Five magnetic models (four antiferromagnetic and one ferromagnetic) were constructed for a single crystallographic unit cell. The ordering can be seen in Figure 1. In the first, AFI, all closest U−U

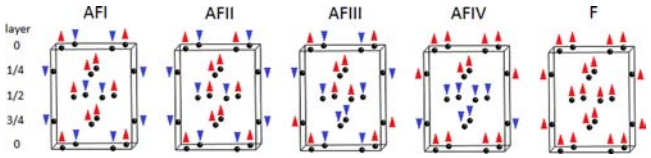

Figure 1. Magnetic ordering of U atoms in $Rb_2Pd_4U_6S_{17}$ used in calculations. Only U atoms are shown. View down [010]. Red triangles represent spin up, and blue represent spin down.

interactions had opposite spins. In the second, AFII, U atoms in layers two and four were aligned as in model AFI and half the atoms in layers one and three were aligned as in model AFI with the other half having the opposite spin. In the third, AFIII, U atoms in layers one and two were aligned as in model AFI and U atoms in layers three and four were aligned opposite to those in model AFI. In the fourth, AFIV, the cell was divided into two halves with U atoms in layers one and two having the same spin and U atoms in layers three and four having the opposite spin. In the fifth, F, all U atoms were aligned ferromagnetically. During the course of self-consistent spin-polarized calculations, all moments were given freedom to relax. As a result, some of the AF states just described proved to be unstable, tending to a ferrimagnetic solution, as described in the Discussion.

DISCUSSION

Syntheses. With the exception of $Cs_2Pd_4U_6Se_{17}$ and $Cs_2Pt_4U_6Se_{17}$, yields were low, with black hexagons of MQ_2[23,24] and poorly formed black needles of β-UQ_2[25,26] as the primary crystalline products. Such behavior is typical for kinetically stable products, where the main products are the thermodynamically stable binary side products.

Structure. The $A_2M_4U_6Q_{17}$ compounds crystallize in a previously unreported structure type with two formula units in the tetragonal space group *P*4/*mnc* (Table 1 and Figure 2). The shortest interatomic Q···Q distances (Table 2) are much longer than a typical single Q−Q bond distance of 2.1 Å for S and 2.3 Å for Se;[27] consequently, there is no Q−Q bonding. Charge balance can thus be achieved by assigning the formal oxidation states A^+, U^{4+}, M^{2+}, and Q^{2-}.

The structure of representative $Rb_2Pd_4U_6S_{17}$ is best understood by slicing it into layers parallel to (001). The first layer, $^2_\infty[Pd_4U_4S_{17}]$ (Figure 3), is composed of $[Pd_4U_4S_{25}]$ units centered at the origin. Each unit contains four monocapped trigonal-prismatic US_7 and four square-planar PdS_4 units. The $[Pd_4U_4S_{25}]$ unit has 4-fold rotational symmetry. The four US_7 units share the capping S3 atom, which sits at the origin. Each US_7 unit shares two triangular faces on the cap, one with each neighbor. The two rectangular faces of the US_7 units are perpendicular to the basal plane. The four edges common to a rectangular face and a capping face are also shared with PdS_4 units. The planes of the PdS_4 units are coplanar with the central capping S3 atom. This $[Pd_4U_4S_{25}]$ unit can be compared to a wheel with spokes. The unit is rotated so the spokes are about 20° from the *a* and *b* axes. Each $[Pd_4U_4S_{25}]$

dx.doi.org/10.1021/ic300865y | Inorg. Chem. 2012, 51, 8873−8881

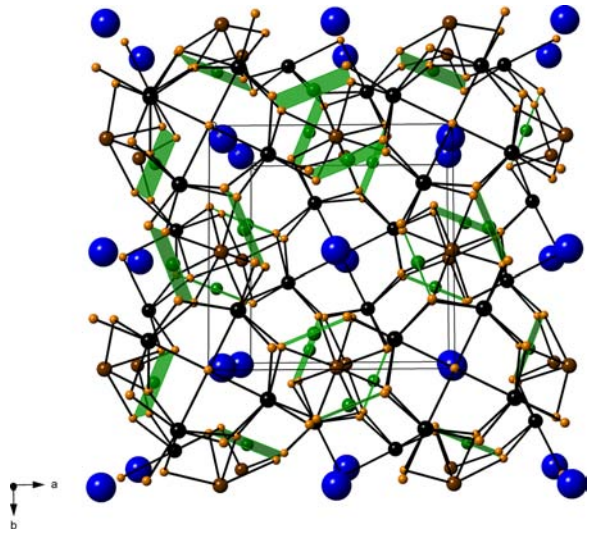

Figure 2. Structure of $Rb_2Pd_4U_6S_{17}$ structure viewed down [010]. Rb atoms are blue, U1 atoms are black, U2 atoms are brown, Pd atoms are green, and S atoms are orange.

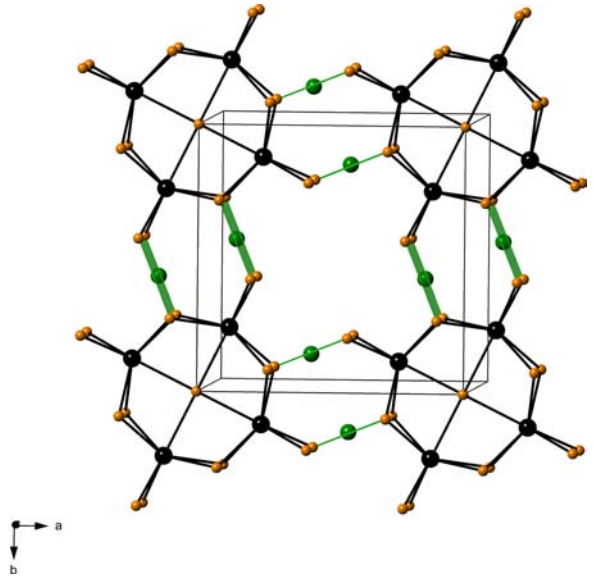

Figure 3. $^2_\infty[Pd_4U_4S_{17}]$ layer at $z = 0$ viewed down [001]. U1 atoms are black, Pd squares are green, and S atoms are orange.

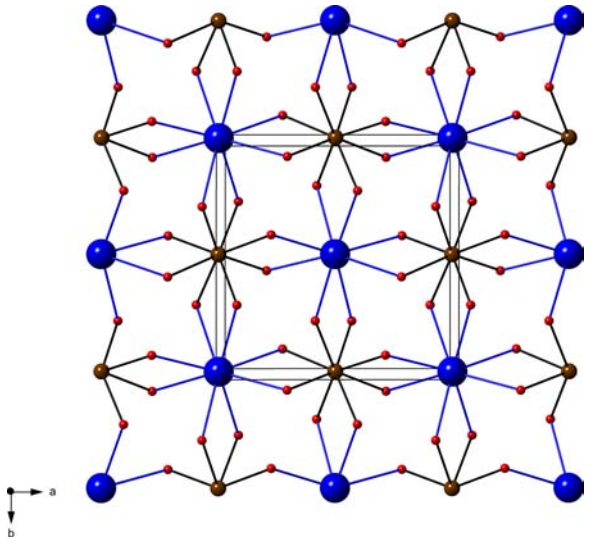

Figure 4. $^2_\infty[Rb_2U_2S_{16}]$ layer at $z = 0.25$ viewed down [001]. Rb atoms are blue, U2 atoms are brown, and S atoms are orange.

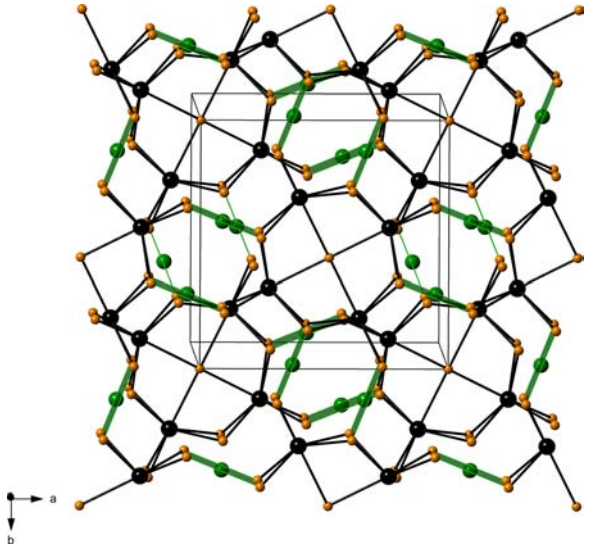

Figure 5. Stacking of $^2_\infty[Pd_4U_4S_{17}]$ layers. $^2_\infty[Rb_2U_2S_{16}]$ layers are omitted. U1 atoms are black, U2 atoms are brown, Pd atoms are green, and S atoms are orange.

unit is connected to four adjacent units by sharing the far edge of the $Pd1S_4$ units with the $U1S_7$ edge common to the two rectangular faces. Large voids remain at (1/2, 1/2, 1/2).

The second layer, $^2_\infty[Rb_2U_2S_{16}]$ (Figure 4), contains $U2S_8$ square antiprisms and $Rb1S_9$ monocapped square antiprisms. These units are arranged in a checkerboard pattern, where the $U2S_8$ units are the black squares, and the $Rb1S_9$ units are the white squares. These units edge-share along the "crowns" of the antiprisms, on edges shared by triangular faces. The $Rb1S_9$ units are further divided into two square sublattices. In one, the cap points upward, whereas in the other, it points downward.

The third layer is as the first layer but inverted such that the Rb-capping S3 atom of the other square lattice is over the large void left in the first layer, when looking down [001]. Also, the Pd squares are rotated 70° from the *a* and *b* axes (Figure 5).

The fourth layer is like the second layer but is also inverted relative to the second layer. As a result, the $Rb1S_9$ sublattices alternate, i.e., where the $Rb1S_9$ cap points upward; in the next layer the $Rb1S_9$ cap points downward.

The layers are connected as follows: The $Pd1S_4$ edges in the basal plane are shared with the square face of the $U2S_8$ square antiprisms in both adjacent layers. That is, the $U2S_8$ square antiprism shares two parallel edges on each square face with $Pd1S_4$ units. The S3 atom is shared among four $U1S_7$ units and two $Rb1S_9$ units. Each of the four triangular capping faces of the $Rb1S_9$ unit is shared with a $U1S_7$ unit.

The coordination environments of the U atoms are shown in Figure 6. Monocapped trigonal-prismatic coordination (Figure 6a) may be considered a distortion of the seven-coordinate triangle+rectangle found in PdU_2S_4 and also U_3S_5.[28,29] Square antiprismatic coordination (Figure 6b) has not been previously reported for uranium chalcogenides but is found in other uranium compounds such as CuUOP.[30]

Interatomic distances are typical for the coordinations and valencies of the metals: U1−S_7 distances range from 2.680(1) Å

dx.doi.org/10.1021/ic300865y | *Inorg. Chem.* 2012, 51, 8873−8881

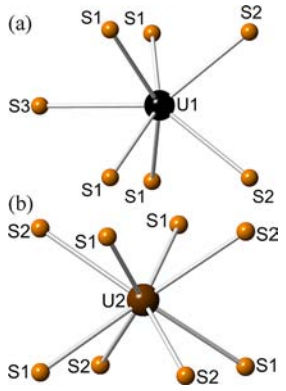

Figure 6. Coordination environments of U1 (a) and U2 (b) in $Rb_2Pd_4U_6S_{17}$.

to 2.823(1) Å vs 2.663 Å to 2.858 Å in U_3S_5;[28] U2−S_8 distances range from 2.762(1) Å to 2.887(1) Å vs 2.709(3) Å to 3.033(4) Å in FeU_8S_{17};[31] nine-coordinate Rb1−S distances range from 3.279(1) Å to 3.589(1) Å vs 3.34(1) Å to 3.3782(8) Å in Rb_2AuSbS_4;[32] and square-planar Pd1−S distances of 2.341(1) Å to 2.363(1) Å do not differ from those of 2.32 Å to 2.36 Å found in $Cs_2Pd_3S_4$.[33]

In $Rb_2Pt_4U_6Se_{17}$ and $Cs_2Pt_4U_6Se_{17}$, the A atom disorders over two positions, A1 and A2, along the *c* axis. Taking $Rb_2Pt_4U_6Se_{17}$ as an example, the Rb2 site is 0.799(5) Å away along the *c* axis from its symmetry equivalent generated by a mirror plane (Rb2′). The Rb2 site is within two crystal radii[34] of the Rb1 site, so the Rb2 and the Rb1 sites cannot be occupied simultaneously (Figure 7). The same applies to Rb2′

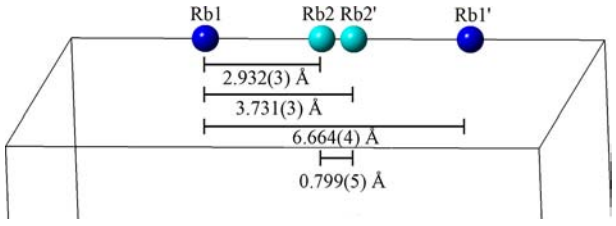

Figure 7. Schematic of the Rb atom disorder in $Rb_2Pt_4U_6Se_{17}$. The only possible arrangements are Rb1 and Rb2′ or Rb1′ and Rb2.

and Rb1′. Instead, only Rb1 and Rb2 sites on opposite sides of the mirror plane may be occupied simultaneously, i.e., either Rb1 and Rb2′ or Rb1′ and Rb2. All of the atom pairs are disordered in this manner. The closest distance between Rb atoms in different atom pairs is 6.741(4) Å. Examination of the data shows no evidence of long-range order. The A1−Se distances are shorter in $A_2Pt_4U_6Se_{17}$ than in $A_2Pd_4U_6Se_{17}$ as seen in Table 2, consistent with the reduced occupancy of the A1 site. Although it is not clear why there is this disorder only in $Rb_2Pt_4U_6Se_{17}$ and $Cs_2Pt_4U_6Se_{17}$, the only factor unique to these compounds is the presence of Pt.

Electrical Resistivity of $Rb_2Pd_4U_6S_{17}$. Figure 8 shows the temperature dependence of the electrical resistivity of $Rb_2Pd_4U_6S_{17}$ along the *c* axis. The temperature dependence shows typical semiconductor behavior. The plot was fit to the Arrhenius formula for thermally activated electrical conductivity, $\rho(T) \propto e^{(E_a/k_BT)}$, where E_a is the activation energy. The slope of the linear fit of lnρ versus $1/T$ corresponds to E_a = 0.09 eV.

Magnetic Susceptibility and Specific Heat of $Rb_2Pd_4U_6S_{17}$. A plot of $\chi(T)$ vs T for $Rb_2Pd_4U_6S_{17}$ is

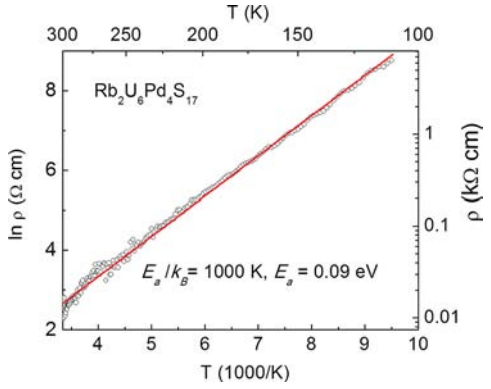

Figure 8. Electrical resistivity (ρ) versus T of $Rb_2Pd_4U_6S_{17}$. Both the linear plot of lnρ versus T^{-1} (bottom-left) and the nonlinear plot of ρ versus T (top-right) correspond to the curve shown. The solid line corresponds the linear fit of the ln ρ versus T^{-1} plot.

presented as an inset in Figure 9. The plot contains a large peak at 16 (17) K, along the *a* (or *b*) and *c* axes. The shape of the curve is characteristic of antiferromagnetic ordering, though the peak lacks the sharp cusp typically seen for such ordering. The peak temperature decreases with increased external field (inset). The data above the peak were fit to the modified Curie−Weiss law, $\chi = C/(T - \theta) + \chi_0$, by plotting χ^{-1} against T (Figure 9), where θ is the Weiss temperature, χ_0 is the temperature-independent magnetic susceptibility, and C is the Curie temperature. The effective magnetic moment is given by the relationship $\mu_{eff} = (8C)^{1/2}$. These fitting parameters are tabulated in Table 3.

The effective magnetic moments of 2.36−2.45 μ_B, though less than the free-ion value for U^{4+} of 3.6 μ_B, are not unusual in inorganic compounds. For instance, in $Ba_2Cu_2US_5$, the magnetic moment of U^{4+} is 2.69(2) μ_B,[35] and in $Cu_2U_3S_7$, it is 2.50 μ_B.[36] Crystalline electric field (CEF) effects were cited as the source of the reduced magnetic moments for these compounds. The compound $Rb_2Pd_4U_6S_{17}$ is a semiconductor, and hence, the f electrons are localized. Thus, we conclude that the reduced magnetic moment results from CEF effects.

Heat capacity measurements were carried out to investigate the thermodynamic origin of the magnetic susceptibility peak (Figure 10). The λ-shaped jump of the heat capacity with a peak at 13.0 K suggests that the magnetic susceptibility maximum is indeed the result of a phase transition involving long-range ordering. The entropy change (ΔS) associated with the phase transition was determined from the relation $\Delta S = \int (C_p - C_{ph})/T \, dT$, where C_{ph} is the lattice contribution to the heat capacity. Using an empirical curve for the lattice contribution shown in Figure 10, we obtained $\Delta S = 0.5\ R$ (R = 8.31 J/K mol). For long-range ordering of magnetic ions with total angular momentum J, ΔS is expressed as $\Delta S = R \ln (2J + 1)$. In $Rb_2Pd_4U_6S_{17}$, there are six U atoms in the formula unit, which leads to $\Delta S = 6\ R \ln (2J + 1)$ for a complete ordering of the six U^{4+} moments. Then, we can estimate the J value by equating this formula to the observed ΔS value of 0.5 R to obtain J = 0.04. This value is too low for a phase transition involving long-range magnetic ordering, even when account is taken of the reduced effective moment that results from CEF effects.

Antiferromagnetic ordering is supported by the negative Weiss temperature and its suppression by external fields. In this case, the Néel temperature (T_N) may be lower than the

dx.doi.org/10.1021/ic300865y | Inorg. Chem. 2012, 51, 8873−8881

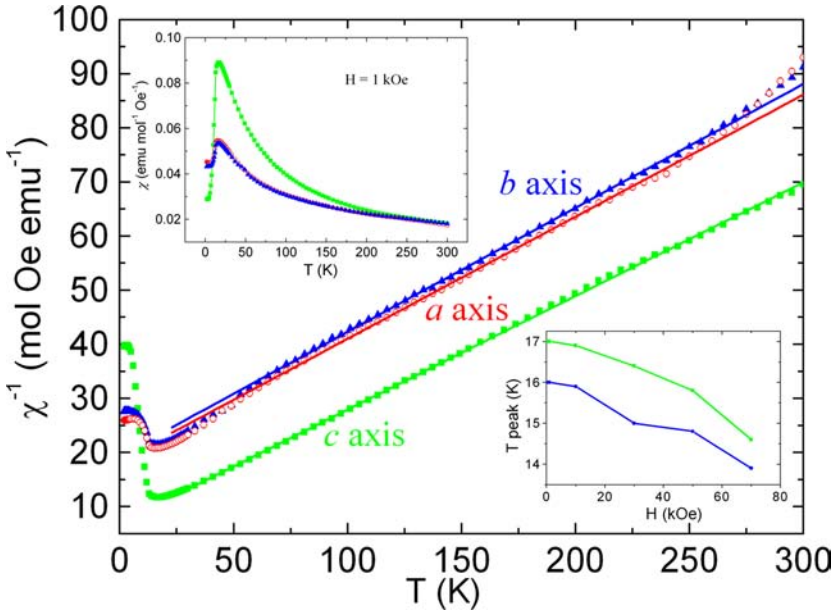

Figure 9. χ^{-1} versus T along the three crystallographic axes of $Rb_2Pd_4U_6S_{17}$. Linear fits are shown with solid lines. Magnetic susceptibility (χ) versus T along the three crystallographic axes is shown as an inset as is the change in susceptibility peak temperature as a function of applied field (H) along the b and c axes.

Table 3. Magnetic Behavior of $Rb_2Pd_4U_6S_{17}$

	c axis	b axis	a axis
T_N (K)	17	16	16
μ_{eff}/U (μ_B)	2.36	2.43	2.45
θ (K)	−32	−84	−82
χ_0 (emu mol^{-1} Oe^{1-})	4.6×10^{-3}	8.0×10^{-3}	7.5×10^{-3}

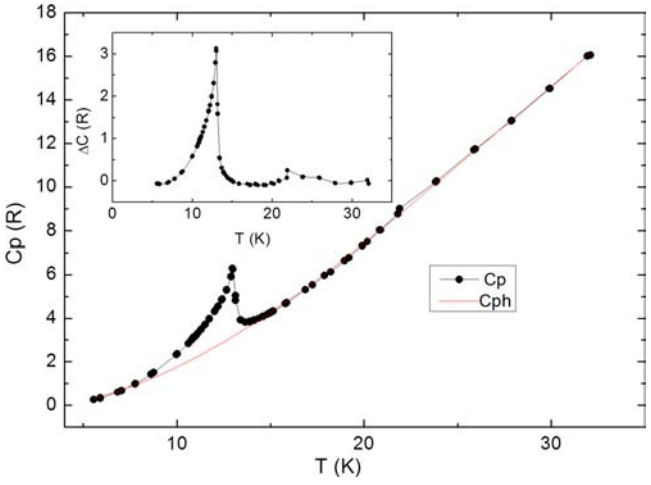

Figure 10. Heat capacity of $Rb_2U_6Pd_4S_{17}$ at zero magnetic field. The inset shows the specific heat after the phonon contribution (C_{ph}) is subtracted ($\Delta C = C_p - C_{ph}$).

observed susceptibility peak temperature and should be close to the peak temperature of the heat capacity. A value of T_N = 12.5, closer to the heat capacity peak at 13 K, was more accurately determined by finding the peak of the $d(\chi T)/dT$ vs T curve[37] (Figure 11)

The weak anisotropy of the magnetic susceptibility below the peak temperature occurs because either (1) the easy magnetization axis does not coincide with any crystallographic axis or (2) the spins are canted in the antiferromagnetic regime. Such

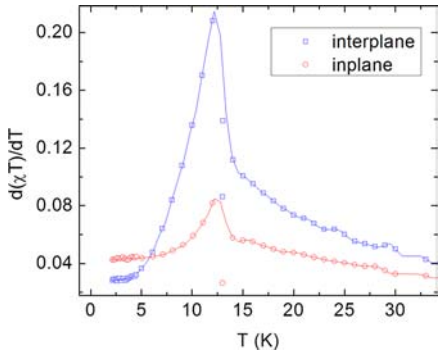

Figure 11. $d(\chi T)/dT$ as a function of temperature for $Rb_2Pd_4U_6S_{17}$. The solid line is a guide for the eye.

behavior is also found in UPdSn.[38,39] Magnetization plots (Figure 12) are insufficient to determine the cause of this susceptibility decrease below the transition temperature. The magnetization plots show divergence from linearity above 10 kOe along the a and b axes and 30 kOe along the c axis; this is indicative of a possible spin-flop-like transition. This divergence occurs at lower fields along the a and b axes, suggesting the antiferromagnetic easy axis is in the basal plane. The a- and b-axis measurements are nearly identical, consistent with the tetragonal symmetry of the structure. Minor magnetic anisotropy is evident when comparing the c-axis measurement to the a- and b-axis measurements.

Another possible source of the peak in the temperature dependence of the specific heat is a structural phase transition rather than a magnetic ordering transition. The small ΔS and the weak anisotropy of the magnetic susceptibility below the peak temperature are better explained by a structural phase transition. Given that the crystals do not shatter as the temperature is lowered, such a transition would most likely have to be second order. Short of diffraction studies of $Rb_2Pd_4U_6S_{17}$ below the transition temperature, there is no clear

dx.doi.org/10.1021/ic300865y | Inorg. Chem. 2012, 51, 8873−8881

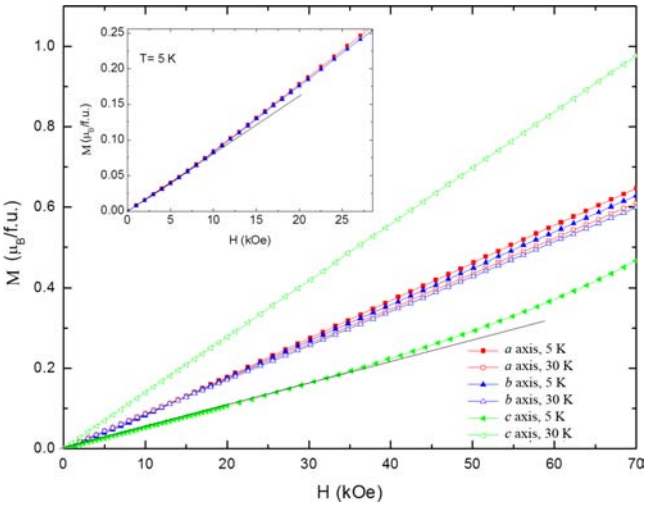

Figure 12. Magnetization plots of μ_{eff}/fomula unit vs external field along the three axes of $Rb_2Pd_4U_6S_{17}$. Lines emphasize divergence from linearity. Inset shows low-field behavior.

choice to be made between a structural vs magnetic phase transition.

Bond Valences. Calculated bond valence sums for $Rb_2Pd_4U_6S_{17}$ for the atoms Rb1, Pd1, U1, U2, S1, S2, and S3 are +1.30, +2.03, +4.07, +3.97, −2.05, −2.03, and −2.29, respectively. The compound consequently may be written-$(Rb^+)_2(Pd^{2+})_4(U^{4+})_6(S^{2-})_{17}$.

Density of States. Plots of the partial densities of states (PDOS) for each atom type in $Rb_2Pd_4U_6S_{17}$ for the spin-polarized antiferromagnetic state AFII are presented in Figure 13. The figure compares the PDOS of a different element: positive values are for spin up, negative values represent spin down. The PDOS are further separated into contributions for orbitals of s, p, d, and f character. It is well-known that the introduction of intra-atomic U f-f correlations can open a gap between the occupied and vacant f-states, correcting a defect in the DFT ground state potential. The GGA+U scheme,[20] with a single empirical parameter, is well suited for this purpose; post-SCF calculations were performed with the Coulomb correlation parameter U set to 4 eV for U f-states. As a result, the occupied-vacant direct band gap opens to 0.91 eV, with both Pd and S excited state features being pushed to higher energy along with the U f-states. The indirect band gaps also increase, beginning at 0.79 eV, leading to a prediction of a narrow-gap semiconductor in agreement with experiment.

Except for the excited state band shifts, the PDOS shapes and intensities are essentially identical for ground state and GGA+U models. In the following, the GGA+U energies are reported. The upper valence band states from 0 to −5 eV are almost exclusively due to d-orbitals of Pd and p-orbitals of S; these heavily overlap suggesting strong hybridizations between these orbitals. At approximately −10 eV, one finds a narrow (∼ 1 eV) band with a large Rb p-orbital contribution and near zero contribution from the S s-orbital. Starting at −11 eV, there is a ∼ 2 eV band with only an S s-orbital attributed to mostly S−S interactions. The lowest valence band occurs from −18 to −20 eV and consists of a large contribution from the p-orbitals of U and a non-negligible contribution from S orbitals. The bands from 1 to 3 eV above E_F consist mostly of U f-orbitals, with a small contribution from Pd d-orbitals and S p- and d-orbitals.

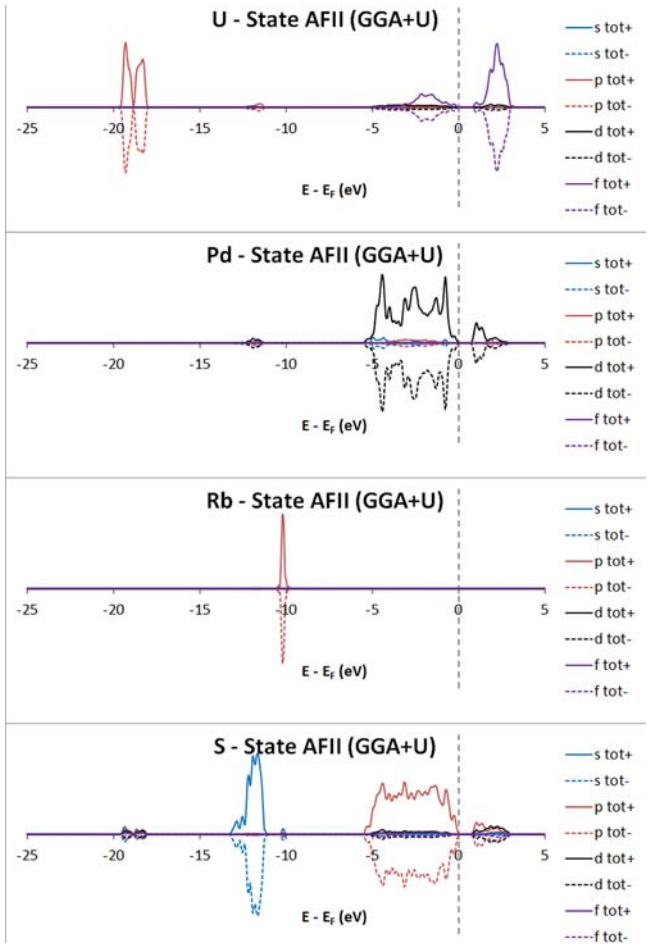

Figure 13. Density of states for $Rb_2Pd_4U_6S_{17}$ in the antiferromagnetic state AFII within the GGA+U formalism.

Magnetic Calculations. Spin-polarized calculations resulted in the ferromagnetic state, F, as the lowest in energy at −387.13 eV/cell. All antiferromagnetic states were higher in energy. The relative energies of all five states can be found in Table 4. Upon introduction of spin−orbit coupling (SOC), the calculated absolute energies decreased by approximately 40 eV. The ferromagnetic state was again lowest in energy at −425.44 eV/cell with all antiferromagnetic states being higher in energy. The relative energies of all five states can be found in Table 4. It is possible that a calculation involving a larger magnetic supercell would reveal a lower antiferromagnetic energy state. The final magnetizations reported in Table 5 show that AFI, II,

Table 4. Calculated Total Energies Relative to the Lowest Energy Structure

$Rb_2Pd_4U_6S_{17}$	AFI	AFII	AFIII	AFIV	F
ΔE^a	0.86	0.79	1.71	0.18	0
ΔE^b	0.40	0.38	0.90	0.20	0

[a]Spin polarized calculations. [b]Spin−orbit coupling calculations.

Table 5. Final Magnetization (μ_B/U atom)

$Rb_2Pd_4U_6S_{17}$	AFI	AFII	AFIII	AFIV	F
all U atoms	−0.30	−0.68	−0.14	0.00	1.74
all atoms	−0.31	−0.70	−0.15	0.00	1.80

dx.doi.org/10.1021/ic300865y | Inorg. Chem. 2012, 51, 8873−8881

and III were unstable to spin rotations into a ferrimagnetic state. The initial self-consistent calculations (and energies given in Table 4) represent metastable AF configurations.

Only AFIV resisted a small perturbation, which caused the "decay" of AFI, II, and III. Although only very limited experimentation was done with a potentially large number of initial boundary conditions, we take the results to indicate a tendency toward the F ground state, consistent with the calculated energies. The U f charge and spin contributions were calculated for each state by a spherical volume integration (radius R_W = 1.50 Å), giving an occupation of 2.49−2.52 e^-, essentially independent of magnetic state, as would be expected. The U f spin moments vary considerably from one state to another, indicating considerable mutual coupling, possibly via superexchange through S ligands. For the F ground state, the f spin ranges over 1.66−1.74 μ_B for inequivalent sites, with a net spin moment of 22.09 μ_B. The effective moment per U atom, 22.09/12 = 1.84 μ_B, shows a non-negligible contribution of polarized Pd atoms, which is verified by an integrated Pd spin moment of ∼0.05 μ_B.

Spin−orbit coupling was treated post-SCF by a perturbative method for a number of different initial moment orientations and magnitudes. When the spin axis was constrained to lie along the crystal *c*-axis, the "ferromagnetic" state was again found to be lowest in energy. However, when the initial spin axis was canted, e.g., along [100], then convergence to several canted magnetic configurations with lower energy was found with energy differences ∼250 meV/cell. With present limitations on the size of a magnetic unit cell and computational facilities, it is not feasible to carry out extensive searches for the true ground state.

CONCLUSIONS

Reactions of U, M, Q, and Rb_2S_3 or ACl yield six compounds with formulas $A_2M_4U_6Q_{17}$ (A = Rb or Cs; M = Pd or Pt; Q = S or Se). These compounds crystallize in a new structure type in the tetragonal space group *P*4/*mnc*. This structure consists of a network of square-planar MQ_4, monocapped trigonal-prismatic UQ_7, and square-antiprismatic UQ_8 polyhedra with A atoms in the voids.

Periodic spin-polarized band structure calculations were performed on $Rb_2Pd_4U_6S_{17}$ with the use of the first principles DFT program VASP. Magnetic calculations included spin−orbit coupling. U f-f correlations were taken into account within the GGA+U formalism in calculating partial densities of states. The compound is predicted to be a narrow-band semiconductor with the smallest indirect and direct band gaps being 0.79 and 0.91 eV, respectively.

The electrical resistivity of a single crystal of $Rb_2Pd_4U_6S_{17}$ along the *c* axis shows typical semiconductor behavior with a thermal activation energy of 0.09 eV. This result is in qualitative agreement with PDOS calculations, which also predict semiconductor behavior.

Even with extensive single-crystal magnetic measurements as well as heat capacity measurements on $Rb_2Pd_4U_6S_{17}$, there remain uncertainties about the behavior of the compound at low temperatures. There is a peak at about 16 K in the magnetic susceptibility vs temperature. Above 16 K, the data may be fit to the modified Curie−Weiss law to afford values of μ_{eff}/U of 2.36−2.45 μ_B . The negative Weiss constant and its suppression by external fields are consistent with antiferromagnetic ordering. The weak anisotropy of the magnetic susceptibility below the peak temperature could occur because the easy magnetization axis does not coincide with any crystallographic axis. The magnetization plots show divergence from linearity above 10 kOe along the *a* and *b* axes and 30 kOe along the *c* axis. This could arise from a possible spin-flop transition, in turn because the easy axis was not aligned with the external magnetic fields, which were placed along the crystallographic axes. Alternatively, the weak anisotropy could be a result of the spins canting in the antiferromagnetic regime. The net result would be ferrimagnetism, which is supported by the calculations.

The negative λ-shaped jump of the heat capacity with a peak at 13 K suggests to us that the magnetic susceptibility maximum is indeed the result of a phase transition involving long-range ordering. However, the derived total angular momentum J = 0.04 is too low to be associated with long-range ordering of magnetic ions. Another possible source of the peak in the temperature dependence of the specific heat is a structural phase transition rather than a magnetic ordering transition. The small ΔS and the weak anisotropy of the magnetic susceptibility below the peak temperature support this argument. Short of diffraction studies of $Rb_2Pd_4U_6S_{17}$ below the transition temperature there is no clear choice to be made between a structural vs a magnetic phase transition.

ASSOCIATED CONTENT

Supporting Information

Crystallographic files in cif format for all six compounds. This material is available free of charge via the Internet at http://pubs.acs.org

AUTHOR INFORMATION

Corresponding Author

*E-mail: ibers@chem.northwestern.edu.

Notes

The authors declare no competing financial interest.

ACKNOWLEDGMENTS

The work presented was supported by the U.S. Department of Energy, Basic Energy Sciences, Chemical Sciences, Biosciences, and Geosciences Division and Division of Materials Science and Engineering Grant ER-15522. A portion of this work was performed at the National High Magnetic Field Laboratory, which is supported by NSF Cooperative Agreement No. DMR-0654118, by the State of Florida, and by the DOE. SEM analyses were conducted in the Electron Probe Instrumentation Center (EPIC) at the Northwestern University Atomic and Nanoscale Characterization Experimental (NUANCE) Center, supported by NSF-NSEC, NSF-MRSEC, Keck Foundation, the State of Illinois, and Northwestern University. Crystallographic data were collected at the IMSERC X-ray Facility at Northwestern University, supported by the International Institute of Nanotechnology (IIN). Use was made of the Magnet and Low Temperature facility operated by the NSF-supported Northwestern University Materials Research Center. L.A.K. was also supported by the Nuclear Energy University Programs of the U.S. Department of Energy Office of Nuclear Energy.

REFERENCES

(1) Oh, G. N.; Ibers, J. A. *Acta Crystallogr.* **2011**, *E67*, i9.
(2) Oh, G. N.; Choi, E. S.; Ibers, J. A. *Inorg. Chem.* **2012**, *51*, 4224−4230.

(3) Tams, G.; Müller-Buschbaum, H. *Z. Anorg. Allg. Chem.* **1992**, *617*, 19−22.
(4) Yao, J.; Ibers, J. A. *Z. Anorg. Allg. Chem.* **2008**, *634*, 1645−1647.
(5) Cody, J. A.; Ibers, J. A. *Inorg. Chem.* **1995**, *34*, 3165−3172.
(6) Bugaris, D. E.; Ibers, J. A. *J. Solid State Chem.* **2008**, *181*, 3189−3193.
(7) Haneveld, A. J. K.; Jellinek, F. *J. Less-Common Met.* **1969**, *18*, 123−129.
(8) Sunshine, S. A.; Kang, D.; Ibers, J. A. *Mater. Res. Soc. Symp. Proc.* **1987**, *97*, 391−396.
(9) *Bruker APEX2 Version 2009.5−1 and SAINT version 7.34a Data Collection and Processing Software*; Bruker Analytical X-Ray Instruments, Inc.: Madison, WI, 2009.
(10) Sheldrick, G. M. *SADABS*; Department of Structural Chemistry, University of Göttingen, Göttingen, Germany, 2008.
(11) Sheldrick, G. M. *Acta Crystallogr., Sect. A: Found. Crystallogr.* **2008**, *64*, 112−122.
(12) Gelato, L. M.; Parthé, E. *J. Appl. Crystallogr.* **1987**, *20*, 139−143.
(13) Spek, A. L. PLATON, a Multipurpose Crystallographic Tool; Utrecht University, Utrecht, The Netherlands, 2008.
(14) Brese, N. E.; O'Keeffe, M. *Acta Crystallogr., Sect. B: Struct. Sci.* **1991**, *47*, 192−197.
(15) Kresse, G.; Hafner, J. *Phys. Rev. B* **1993**, *47*, 558−561.
(16) Kresse, G.; Hafner, J. *Phys. Rev. B* **1994**, *49*, 14251−14271.
(17) Kresse, G.; Forthmüller, J. *Comput. Mater. Sci.* **1996**, *6*, 15−50.
(18) Kresse, G.; Furthmüller, J. *Phys. Rev. B* **1996**, *54*, 11169−11186.
(19) Kresse, G.; Joubert, D. *Phys. Rev. B* **1999**, *59*, 1758−1775.
(20) Hubbard, J. *Proc. R. Soc. London, Ser. A* **1963**, *276*, 238−257.
(21) Monkhorst, H. J.; Pack, J. D. *Phys. Rev. B* **1976**, *13*, 5188−5192.
(22) Fazekas, P. *Series in Modern Condensed Matter Physics: Lecture Notes on Electron Correlation and Magnetism*; World Scientific Publishing Co. Pte. Ltd.: River Edge, NJ, 1999; Vol. *5*.
(23) Grønvold, F.; Røst, E. *Acta Crystallogr.* **1957**, *10*, 329−331.
(24) Furuseth, S.; Selte, K.; Kjekshus, A. *Acta Chem. Scand.* **1965**, *19*, 257−258.
(25) Suski, W.; Gibinski, T.; Wojakowski, A.; Czopnik, A. *Phys. Status Solidi A* **1972**, *9*, 653−658.
(26) Noël, H.; Potel, M.; Troc, R.; Shlyk, L. *J. Solid State Chem.* **1996**, *126*, 22−26.
(27) Böttcher, P. *Z. Anorg. Allg. Chem.* **1977**, *432*, 167−172.
(28) Potel, M.; Brochu, R.; Padiou, J.; Grandjean, D. *C. R. Seances Acad. Sci., Ser. C* **1972**, *275*, 1419−1421.
(29) Noël, H.; Prigent, J. *Physica B+C* **1980**, *102*, 372−379.
(30) Kaczorowski, D.; Albering, J. H.; Noël, H.; Jeitschko, W. *J. Alloys Compd.* **1994**, *216*, 117−121.
(31) Kohlmann, H.; Stöwe, K.; Beck, H. P. *Z. Anorg. Allg. Chem.* **1997**, *623*, 897−900.
(32) Hanko, J. A.; Kanatzidis, M. G. *J. Alloys Compd.* **1998**, *280*, 71−76.
(33) Bronger, W.; Huster, J. *J. Less-Common Met.* **1971**, *23*, 67−72.
(34) Shannon, R. D. *Acta Crystallogr., Sect. A: Cryst. Phys., Diffr., Theor. Gen. Crystallogr.* **1976**, *32*, 751−767.
(35) Zeng, H.-yi; Yao, J.; Ibers, J. A. *J. Solid State Chem.* **2008**, *181*, 552−555.
(36) Daoudi, A.; Lamire, M.; Levet, J. C.; Noël, H. *J. Solid State Chem.* **1996**, *123*, 331−336.
(37) Fisher, M. E. *Philos. Mag.* **1962**, *7*, 1731−1743.
(38) Nakotte, H.; Brück, E.; de Boer, F. R.; Svoboda, P.; Tuan, N. C.; Havela, L.; Sechovsky, V.; Robinson, R. A. *J. Appl. Phys.* **1993**, *73*, 6551−6553.
(39) de Boer, F. R.; Brück, E.; Nakotte, H.; Andreev, A. V.; Sechovsky, V.; Havela, L.; Nozar, P.; Denissen, C. J. M.; Buschow, K. H. J.; Vaziri, B.; Meissner, M.; Maletta, H.; Rogl, P. *Phys. B* **1992**, *176*, 275−287.

NOTE ADDED AFTER ASAP PUBLICATION

This paper was published on the Web on August 3, 2012. Figure 9 was revised and the corrected version was reposted on August 6, 2012.